AGU PUBLICATIONS

JGR

Journal of Geophysical Research: Space Physics

RESEARCH ARTICLE
10.1002/2015JA022283

Key Points:
- SED-TOI structure varied with energy input to the magnetosphere
- Interconnection between polar TOI and intensive Joule heating
- Their common driver is the merging or geo-effective **E** field

Correspondence to:
I. Horvath,
ihorvath@itee.uq.edu.au

Citation:
Horvath, I., and B. C. Lovell (2016), Polar tongue of ionization (TOI) and associated Joule heating intensification investigated during the magnetically disturbed period of 1–2 October 2001, *J. Geophys. Res. Space Physics*, *121*, 5897–5913, doi:10.1002/2015JA022283.

Received 18 DEC 2015
Accepted 3 JUN 2016
Accepted article online 8 JUN 2016
Published online 29 JUN 2016

Polar tongue of ionization (TOI) and associated Joule heating intensification investigated during the magnetically disturbed period of 1–2 October 2001

Ildiko Horvath[1] and Brian C. Lovell[1]

[1]Security and Surveillance Research Group, School of Information Technology and Electrical Engineering, University of Queensland, Brisbane, Queensland, Australia

Abstract We investigate storm-enhanced density (SED) and polar tongue of ionization (TOI) over North America under southward Interplanetary Magnetic Field conditions. We focus on the 30 September to 1 October 2001 medium magnetic storm's recovery phase (Period 1) and on the last substorm (Period 2) of the following 2 October substorm series. We aim to study the SED-TOI structure in the time frame of solar wind energy input to the magnetosphere-ionosphere system and in terms of Joule heating. We utilize GPS total electron content maps tracking SED plume and polar TOI, and spectrogram images detecting polar rain and precipitation void and thus evidencing dayside merging. The variations of merging electric (**E**) field ($\mathbf{E_M}$) and its mapped-down polar equivalent ($\mathbf{E_P}$), energy input efficiency (EI_{eff}), and modeled Joule heating rate (Q_{Joule}) are monitored. Results show multiple Joule heating intensification points implying multiple energy deposition points at high latitudes where the magnetic pole was one of the preferred locations. During the higher EI_{eff} (~1.5%) Period 2, the polar TOI was associated with a well-defined strong Q_{Joule} intensification and with polar rain (or void) on the dayside (or nightside). During the lower EI_{eff} (~0.5%) Period 1, only weak Q_{Joule} intensification occurred in the absence of both polar TOI and polar rain. We highlight the polar TOI's potential impact on the thermosphere. We conclude that (i) strong ($\mathbf{E_M} \approx 5$ mV/m during Period 2) or weak ($\mathbf{E_M} \approx 0.5$–2 mV/m during Period 1) $\mathbf{E_M}$ facilitated energy deposition close to the magnetic pole and (ii) E_{leff} could be used as a diagnostic of the polar TOI's intensity.

1. Introduction

During geomagnetic storms, solar wind (SW) kinetic energy (U_{SW}) becomes very important to the coupled system of solar wind-magnetosphere-ionosphere-thermosphere (SW-M-I-T). Both the orientation and the magnitude of the interplanetary magnetic field (IMF) control the transfer of U_{SW} to the magnetosphere [*Dungey*, 1961]. More solar wind energy can be transported to the magnetosphere during southward $\mathbf{B_Z}$ than northward $\mathbf{B_Z}$ and during intense southward $\mathbf{B_Z}$ than weak southward $\mathbf{B_Z}$ [*Tsurutani and Gonzalez*, 1997]. As a process associated with M-I coupling, solar produced storm-enhanced density (SED) [*Foster*, 1993] develops on the equatorward edge of the midlatitude trough [*Foster*, 1993]. SED is a distinct narrow region in longitude extending from the evening trough to the dayside cusp and is regarded as the ionospheric signature of plasmaspheric plume [*Foster et al.*, 2002]. Both the polar convection [*Whalen*, 1989] and the subauroral polarization stream (SAPS) electric (**E**) field [*Foster and Burke*, 2002] transport the SED plume plasma poleward and sunward. Also, as part of M-I coupling, SAPS develops. When downward flowing Region-2 (R-2) field-aligned currents (FACs) close with upward R-1 FACs via poleward directed Pedersen closure currents [*Anderson et al.*, 2001], a large poleward directed SAPS **E** field is set up in the low-conductivity region of the midlatitude trough in order to drive the enhanced closure currents [*Foster and Burke*, 2002]. This SAPS **E** field overlaps the outer plasmasphere, becomes enhanced during periods of increased polar convection and "peels off" [*Chappell*, 1972, 1974; *Lanzerotti and Hasegawa*, 1975] or erodes the outer edge of the plasmasphere's boundary layer (PBL) [*Carpenter and Lemaire*, 2004], and provides also field-aligned transport for the erosion plume [*Foster and Burke*, 2002; *Foster and Vo*, 2002]. Thus, the SED's source region lies in the complex region of PBL and therefore SED plumes are the ionospheric signatures of erosion plumes [*Su et al.*, 2001; *Foster et al.*, 2002] (see diagram in Figure 1).

During southward $\mathbf{B_Z}$, the Interplanetary **E** Field (IEF) [*Nishida*, 1968] $\mathbf{E_Y}$ component merges, via dayside reconnection, with the magnetosphere in the polar cap region where the magnetic field lines are open and are connected to the solar wind. According to recent studies [e.g., *Moore et al.*, 2002], dayside

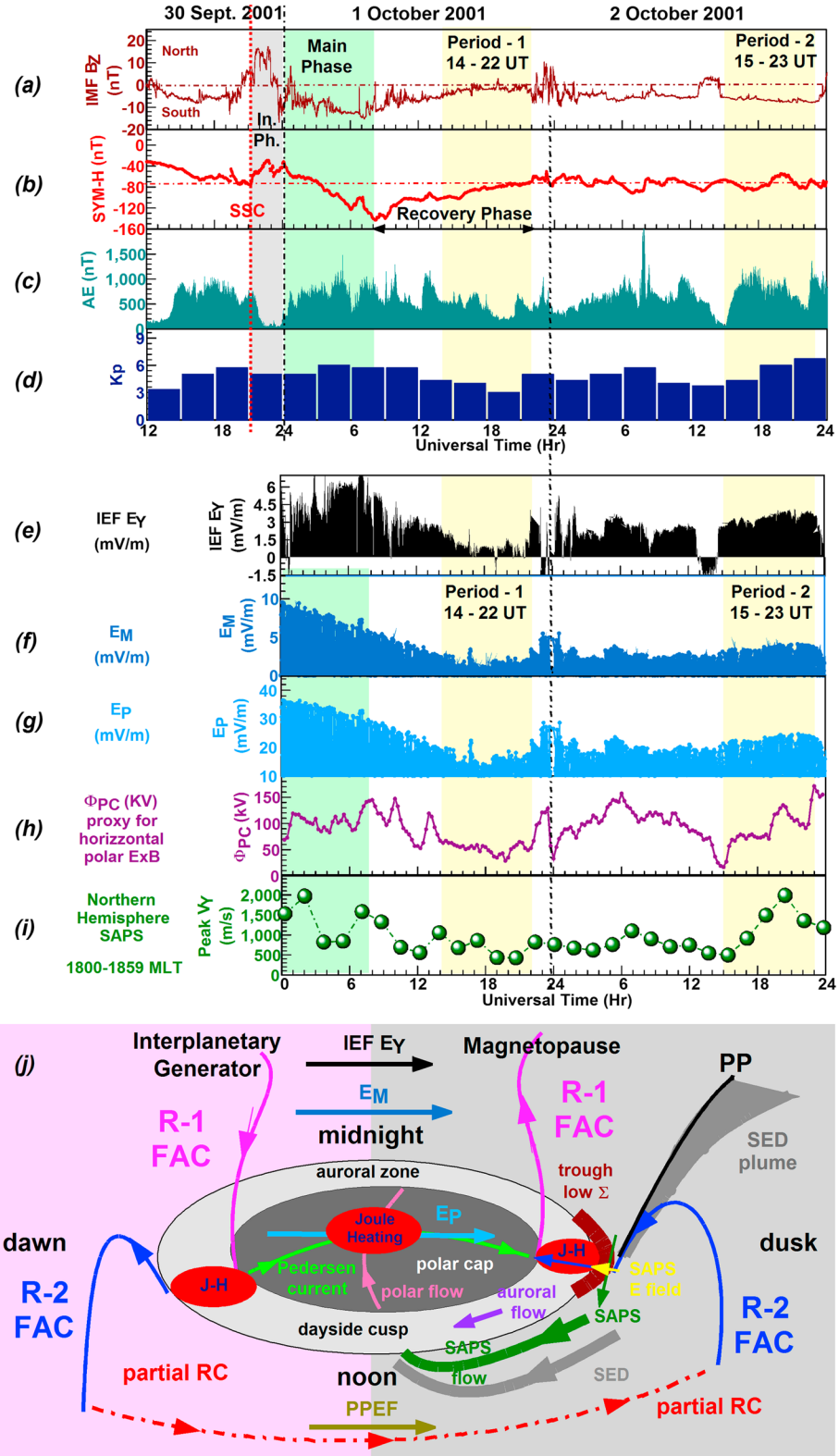

Figure 1. (a–d) The line plots depict a small collection of geophysical variables characterizing the magnetically disturbed period of 30 September to 2 October 2001. The 30 September to 1 October medium magnetic storm was followed by a series of substorms on 2 October. (e–i) The line plots depict the solar wind induced IEF, the merging or geo-effective $\mathbf{E_M}$ and its mapped-down polar **E** field $\mathbf{E_P}$, the cross PCP drop (Φ_{PC}) that is a good proxy for the horizontal polar $\mathbf{E} \times \mathbf{B}$ convection, and the maximum V_Y values at subauroral latitudes representing the SAPS. (j) The diagram, modified after Figure 5 of *Palmroth et al.* [2004], depicts the Joule heating regions and the relations of various **E** fields.

reconnection may occur simultaneously and at different rates in different sectors along the tilted X line or magnetic separator [*Siscoe et al.*, 2000] running through the subsolar region and extending to high latitudes. Dayside reconnection rates are the measure of rate of energy flux transport across the polar cap. Since ionospheric processes are the low-altitude footprints of high-altitude or magnetospheric processes, the polar cap potential (PCP) is a key parameter for describing coupled M-I processes such as the rate of magnetic merging [*Boyle et al.*, 1997]. Dayside merging is governed by a merging or geo-effective **E** field ($\mathbf{E_M}$) [*Kan and Lee*, 1979], and its ionospheric equivalent is known as the polar cap **E** field ($\mathbf{E_P}$) [*Troshichev et al.*, 2000]. $\mathbf{E_M}$ controls both the global energy input and the horizontal polar convection. Under strong horizontal polar convection, when $\mathbf{E_M}$ is intensive, the SED plume has the ability to flow across the dayside cusp region and into the polar cap, and thus to form a polar tongue of ionization (TOI) [*Sato*, 1959; *Sato and Rourke*, 1964]. Combining Super Dual Auroral Radar Network (SuperDARN)-measured polar convection patterns and matching GPS total electron content (TEC) data sets, the formation and movement of polar TOI under superstorm conditions were studied for the first time by *Foster et al.* [2005].

One of the major consumers of magnetospheric energy deposited into the high-latitude ionosphere is Joule heating. Joule heating is resistive heating and is caused by the closure of FACs through the resistive ionosphere. There are two main regions of Joule heating: (1) the polar cap where R-1 FACs close and (2) the auroral oval where R-1 and R-2 FACs close [*Palmroth et al.,* 2004] (see diagram in Figure 1). Joule heating directly increases neutral and ion temperatures in the thermosphere and ionosphere, respectively, and induces pressure gradients. Indirectly, Joule heating contributes to the generation of thermospheric neutral winds and ionosphere dynamo generating disturbance dynamo **E** field (DDEF) [*Blanc and Richmond*, 1980]. Furthermore, Joule heating input to the high-latitude region is regarded to be the primary driver of global perturbations manifested in various ways [*Deng and Ridley*, 2006a]. Altered global circulation patterns in the coupled I-T system are caused by ion drag as a result of direct momentum coupling between ions and neutrals, and become enhanced during magnetically disturbed periods. Then auroral precipitation increases both ionospheric conductivity and the drag coefficient, and ion convection pattern or **E** field is enhanced [*Deng and Ridley*, 2007]. However, the varying nature of **E** field, conductance, and electron density plus the underlying feedback and coupling mechanisms can also significantly increase Joule heating and alter its spatial distribution [*Deng and Ridley*, 2006a].

Joule heating can be assessed by field-aligned Poynting flux measurements [*Kelley et al.*, 1991; *Richmond*, 2010], and changes in ion temperature (Ti) is a good proxy for Joule heating. Investigating the impact of Joule heating on the high-latitude ionosphere is particularly difficult because of the specification of different variables (e.g., conductivity, **E** field, and neutral wind). However, it is well understood that the variability of convection **E** field significantly increases Joule heating in the polar region [*Codrescu et al.*, 1995] and the consequential upward motion lifts the F_2 layer to greater heights [*Deng and Ridley*, 2006b]. Furthermore, highly elevated Ti ($>$4000 K) can increase the recombination rate of O^+, which is Ti dependent, and therefore can lower electron density [*Valladares et al.*, 1998]. Modeling shows that the polar TOI can be (1) eroded and broken into individual patches by Ti larger than 4000 K [*Valladares et al.*, 1994] and (2) enhanced in the topside ionosphere, possibly under lower Ti conditions, by the uplift of F_2 layer to greater heights of lower recombination rates [*Deng and Ridley*, 2006b]

More recently, *Huang et al.* [2014a, 2014b] investigated energy transfer from the magnetosphere to the coupled I-T system during geomagnetic storms by utilizing Poynting flux measurements. According to their Northern Hemisphere results, Poynting flux enhancements at polar and at auroral latitudes were similar. Furthermore, the primary location of thermospheric heating by Joule heat was located at ~83°N (magnetic) latitude in the central polar cap. These new results of *Huang et al.* [2014a, 2014b] demonstrate that the polar cap plays a key role in various M-I-T coupling processes, particularly during magnetic storms.

This study focuses on the SED-TOI structure over North America during the 1–2 October 2001 geomagnetic storm events. We aim to investigate some SED-TOI and SED scenarios plus the underlying energy deposition. Our main goal is to learn about the underlying M-I coupling processes taking place, particularly in the central polar cap. We employ theoretical Joule heating rate values providing information on ion temperature variations and also on the variability of both convection **E** field and ionospheric conductance [*Fujiwara et al.*, 2007]. This study's key ideas are that (1) Joule heating intensifications occurred under southward $\mathbf{B_Z}$ conditions during active dayside merging in the central polar cap, close to the magnetic pole; (2) these Joule heating intensifications became significantly

intensified in the polar TOI region possibly due to the polar TOI-related high convection **E** field and large ionospheric conductivity; and (3) the polar TOI was present (absent) during intensive (weak) dayside merging.

2. Database and Methodology

Our database contains multiinstrument ground- and space-based data and simulations provided by the Thermosphere Ionosphere Electrodynamic General Circulation Model (TIE-GCM).

For monitoring ionospheric conditions, we have utilized Global Positioning System (GPS) total electron content (TEC; total electron content unit (TECU) where 1 TECU = 10^{16} elm^{-2}) values from the global network of 259 ground-based GPS receiver stations operational at that time. These GPS TEC values are from the Madrigal Database of Haystack Observatory and are computed for the mean ionospheric height of 350 km. Multiinstrument in situ measurements are from the Defence Meteorological Satellite Program's (DMSP) spacecraft F13 on 0545–1745 LT orbit at ~840 km altitude. These include ion density (Ni; i$^+$/cm^3), ion, and electron temperature (Ti. Te; K), cross-track plasma drifts (V_Y, V_Z; m/s) in the east-west horizontal or zonal (Y) and north-south or vertical (Z) directions. A small collection of geomagnetic indices monitored the underlying geomagnetic activity. These include the 1 min time resolution *SYM-H* and *AE* data (in nT) plus the 3 h *Kp* values. Ionospheric observations are obtained for the magnetically disturbed days of 1 and 2 October (ΣKp = 38.7 and 39.7, respectively).

For monitoring interplanetary conditions, we have also made use of IMF and various solar plasma measurements taken by the Advanced Composition Explorer (ACE) satellite that was positioned at ~(221.80, −16.37, and −15.24) R_E in GSE coordinate system at the time of sudden storm commencement. Based on this position and the solar wind speed attained at that time, a ~42 min extra time was added to the ACE data allowing comparisons between interplanetary and geomagnetic signatures. By utilizing solar wind velocity ($\mathbf{V_X}$; km/s) and IMF $\mathbf{B_Z}$ (nT) data, the solar motional zonal **E** field, also known as IEF $\mathbf{E}_Y$ (mV/m), was computed as $-\mathbf{V_X} \times \mathbf{B_Z}$ [*Mannucci et al.*, 2005]. By employing the 15 min polar cap north (PCN) index from Thule (77.48°N, 270.93°E (geographic) and 87.68°N (magnetic)), the cross polar cap potential (PCP) drop was modeled as Φ_{PC} (kV) = 20 PCN + 15 that is a good proxy for both the horizontal polar $\mathbf{E} \times \mathbf{B}$ convection [*Stauning*, 2007] and the rates of dayside and nightside reconnection [*Milan et al.*, 2007]. The merging **E** field was computed as $\mathbf{E_M}$ (mV/m)) = $V_{SW}B_T\sin^2(\theta/2)$, where V_{SW} is the solar wind velocity, B_T is the total magnetic field (i.e., $(B_Y{}^2 + B_Z{}^2)^{1/2}$), and $\tan(\theta) = B_Y/B_Z$ [*Kan and Lee*, 1979]. $\mathbf{E_M}$ is created by the merging of IEF with the magnetosphere and thus controls the global magnetospheric energy input and the horizontal polar $\mathbf{E} \times \mathbf{B}$ convection [*Troshichev et al.*, 2000]. $\mathbf{E_M}$'s mapped-down ionospheric equivalent, called polar **E** field ($\mathbf{E_P}$) in the central polar cap region, was computed as $\mathbf{E_P}$ (mV/m) = 9.00 + 4.50 PC − 0.17(PC)^2, where PC = $\mathbf{E_M}$ [*Troshichev et al.*, 2000]. Although many factors determine the state of the ionosphere, this $\mathbf{E_P}$ field can be used to characterize the state of the polar ionosphere, particularly near the magnetic pole [*Troshichev et al.*, 2000]. Auroral oval boundary locations are provided by the Oval Variation Assessment, Tracking, Intensity, and Online Nowcasting (OVATION) project. Via Virginia Tech's interactive plotting tool, we have obtained the values of the Heppner-Maynard Boundary (HMB) in order to get an indication of the polar convection's latitudinal extent [*Heppner and Maynard*, 1987].

For investigating the energetics of the coupled SW-M-I system, we have computed the following parameters. Solar wind kinetic energy (U_{SW}; GW), which is the ultimate source of energy, was computed as U_{SW} (GW) = ½$\rho(V_{SW})^3A$ [*Shue et al.*, 1997] in 10^{+9} W (indicated as GW). Here ρ and V_{SW} are the mass density and the bulk velocity of the solar wind, respectively, and A is the cross section of the dayside magnetosphere by assuming a cylindrical symmetric configuration and taking the magnetotail radius as $X_{GSM} = -30\,R_E$ [*Petrinec and Russell*, 1996]. The epsilon parameter (U_ε; GW) provides an estimation of the total energy input from the solar wind to the magnetosphere and was computed as U_ε (GW) = $(4\pi/\mu_o)V_{SW}B^2(l_o)^2\sin^4(\theta/2)$ [*Perreault and Akasofu*, 1978]. Here μ_o is the magnetic permeability, B is the IMF magnitude computed as $(B_Y{}^2 + B_Z{}^2)^{1/2}$, l_o is 7 R_E, and θ is the clock angle derived from $\tan(\theta) = B_Y/B_Z$ [*Perreault and Akasofu*, 1978; *Akasofu*, 1981]. The energy input efficiency (EI_{eff}; %) from the solar wind to the magnetosphere was computed as $(U_\varepsilon/U_{SW}) \times 100\%$ [*Li et al.*, 2012; *Wang et al.*, 2014]. Finally, we have utilized our online model runs, provided by the Coordinated Community Modeling Center (CCMC). Generated by TIE-GCM (version 1.95), we have employed theoretical Joule heating rate values (Q_{Joule}; W/kg) providing information on Joule heating and ion temperature and also on the variability of both convection **E** field and ionospheric conductance [*Fujiwara et al.*, 2007].

3. Results and Interpretations

3.1. Geomagnetic and Electrodynamic Events of 1–2 October 2001

Figures 1a–1d illustrate time series of IMF $\mathbf{B_Z}$ (nT), *SYM-H* (nT), *AE* (nT), and *Kp* constructed for the time period of 1200 UT 30 September to 2400 UT 2 October 2001. Aiding our analysis, the time intervals of 1400–2200 UT on 1 October and 1500–2300 UT on 2 October are marked as Period 1 and Period 2, respectively. These line plots characterize the prevalent geomagnetic events that include a moderate (*SYM-H* = −148 nT) geomagnetic storm and a series of substorms. On 30 September, the sudden storm commencement (SSC) occurred at ~2100 UT. The following initial phase (2100–0130 UT) and main phase (0130–0830 UT) had been unfolding under southward $\mathbf{B_Z}$ orientation on 1 October. *SYM-H* reached its minimum value of −148 nT and thus registered the onset of the recovery phase at 0830 UT. However, this recovery phase unfolded under southward $\mathbf{B_Z}$ conditions. Although some vigorous $\mathbf{B_Z}$ fluctuations took place between 10 and −10 nT during 2200–2400 UT on 1 October, $\mathbf{B_Z}$ remained mostly southward directed at ~−10 nT on the following day, 2 October. Thus, this southward $\mathbf{B_Z}$ was weaker (~−2 nT) during Period 1 but larger and more constant (~−10 nT) during Period 2. A series of substorms also occurred on 1 and 2 October as indicated by the repeated sudden increases of the *AE* index, reaching ~1000 nT each time. Although *Kp* varied between 3 and 6, it remained close to 6.

Figures 1e–1g illustrate the line plots of IEF $\mathbf{E_Y}$ (i.e., motional solar wind **E** field) and merging **E** field ($\mathbf{E_M}$) for analyzing interplanetary and magnetospheric electrodynamic events, respectively. The line plot of polar **E** field ($\mathbf{E_P}$) illustrates the mapped-down equivalent of $\mathbf{E_M}$. Figure 1h depicts the modeled cross PCP drop (Φ_{PC}) values and shows how the ionospheric horizontal polar convection varied. Figure 1i illustrates with the maximum V_Y values how SAPS varied. We note here the expected close similarities of Figures 1e–1h implying that (1) the motional solar wind **E** field (IEF $\mathbf{E_Y}$) is their primary driver and (2) IEF $\mathbf{E_Y}$ penetrated deep into the magnetosphere as $\mathbf{E_M}$ and then to the polar ionosphere as $\mathbf{E_P}$ and drove the polar convection [*Spiro et al*., 1988]. We also note here the opposite phase between Period 1 and Period 2. While low to minimum values characterize Period 1, medium to high values describe Period 2. Finally, the diagram in Figure 1j shows how these **E** fields are related.

3.2. Ionospheric Response to the 1–2 October 2001 Events During Periods 1 and 2

How the ionosphere responded during the second halves of Period 1 and Period 2 to the above-described **E** field events is illustrated with a series of GPS TEC maps in Figure 2. Arranged in two columns, these regional maps are for the time period of 18–22 UT on 1 October (see Figures 2a–2e) and 2 October (see Figures 2f–2j) providing presentations in hourly intervals. Each TEC map is constructed with 30 min worth of data in order to obtain adequate data coverage. Aiding our analysis, we marked in each map the location of magnetic North Pole plus the local time values at 300°E (geographic) for the American sector and at 120°E for the Australian sector. Furthermore, the features of equatorial ionization anomaly (EIA), SED plume, and polar TOI are labeled (see Figures 2c, 2f, and 2g). To describe them, these maps commonly tracked the two-peak structure of the EIA during the local daytime hours in the American sector and in patches over the Pacific Ocean because of the small amount of ground-based data. Regarding the SED-TOI structure over North America on 2 October (see Figures 2f–2j), a well-developed SED plume was tracked entering the dayside cusp and forming a polar TOI. As each map shows, the polar TOI progressed over the magnetic pole and continued on the nightside as it proceeded antisunward. Oppositely on 1 October over North America (see Figures 2a–2e), only a smaller SED plume developed that stopped progressing further than the dayside cusp. Thus, there was no polar TOI development. Consequently, the polar cap appeared to be a region of low TEC (11–23 TECU; indicated in orange), while TEC minimized (0–11 TECU; indicated in dark brown) over the magnetic pole. The polar TOI's absence (in Period 1) and presence (in Period 2) show also direct correlations with the magnitudes of IEF $\mathbf{E_Y}$, $\mathbf{E_M}$, and $\mathbf{E_P}$; polar convection (Φ_{PC}); and SAPS (see Figures 1e–1i) as indicated by the low to minimum (in Period 1) and median to high (in Period 2) values.

3.3. Joule Heating Source Over the Magnetic North Pole During Periods 1 and 2

Figures 3 and 4 show TIE-GCM-simulated Northern Hemisphere Joule heating rate (Q_{Joule}; W/kg) maps and longitudinal cross sections, respectively, during Periods 1 and 2. Longitudinal variation was tracked along 80°N (geographic) latitude passing through the magnetic North Pole at ~280°E (geographic). All these figures

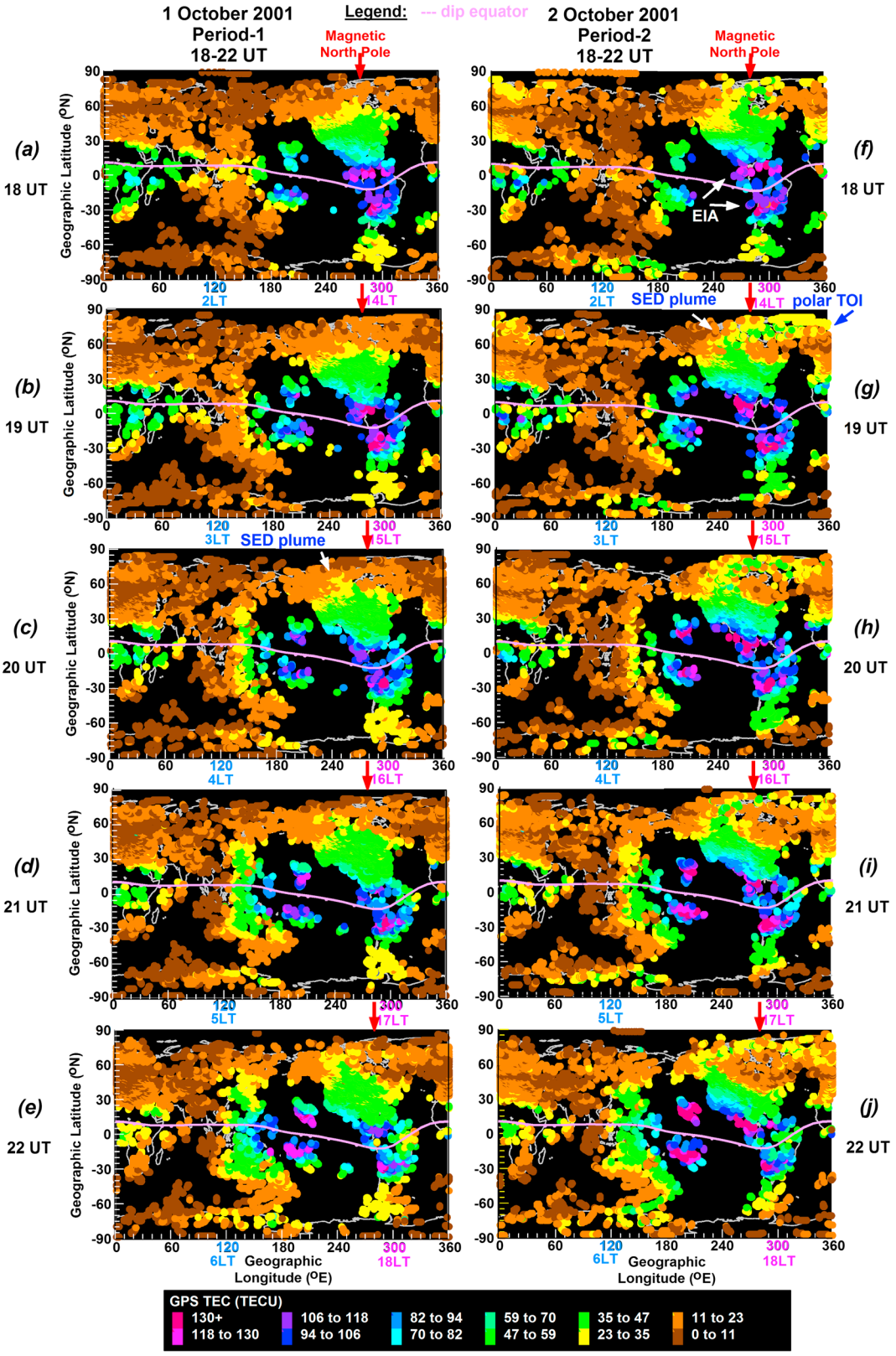

Figure 2. Two sets of GPS TEC maps, constructed with 30 min worth of data, depict the ionosphere's response to the (a–e) 1 October and (f–j) 2 October events. In each map, LT values are indicated for 120°E and 300°E geographic longitudes. The ionospheric features of (Figure 2c) SED plume, (Figure 2f) EIA, and (Figure 2g) SED plume with polar TOI are labeled.

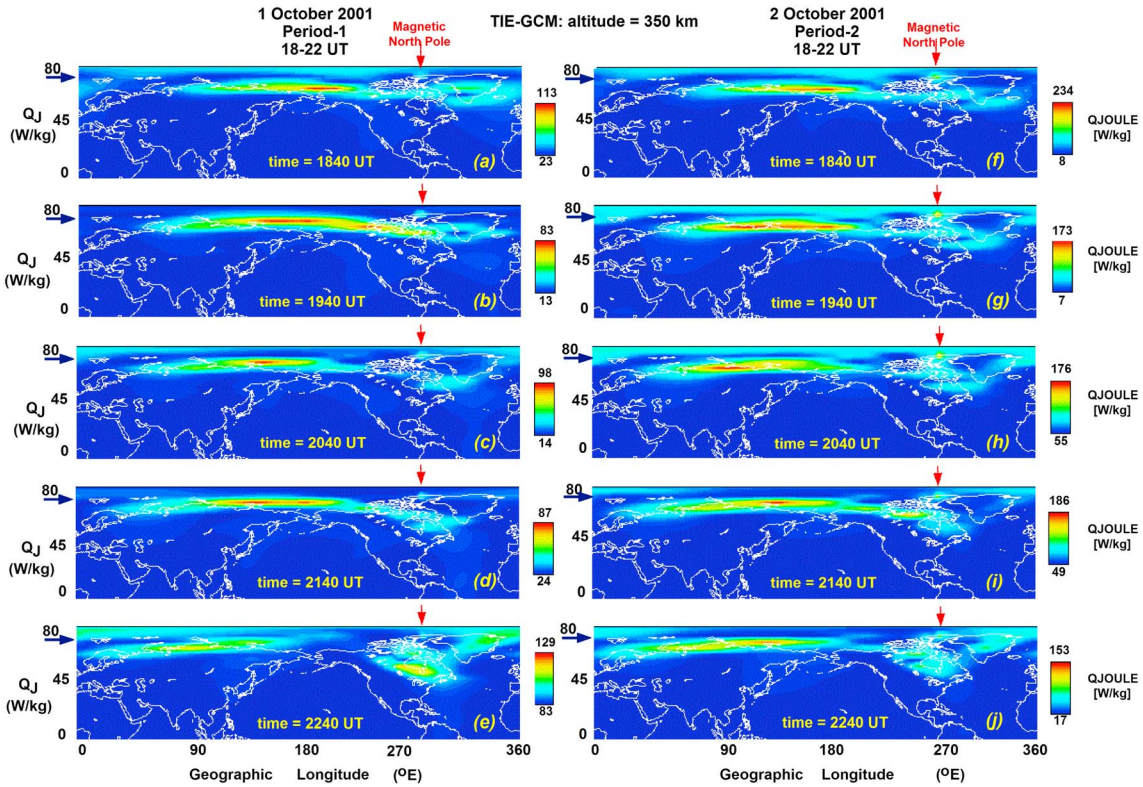

Figure 3. The Q_{Joule} Northern Hemisphere maps are constructed for the GPS TEC maps shown in Figure 2. Over the magnetic pole (a–e) there is only a small Joule heat intensification when the polar TOI was absent, while (f–j) a large and well-defined peak is evident when the polar TOI was present.

are constructed for the UT hours covered by the previously shown GPS TEC maps and for 350 km mean ionospheric height utilized for GPS TEC computation.

Regarding the spatial variations in the 180–360°E sector of our interest, multiple Q_{Joule} intensifications are apparent at auroral and polar latitudes. In Period 2 when the polar TOI was present, these auroral and polar Q_{Joule} intensifications became quite similar (see Figures 3f–3j). Over the magnetic pole, Q_{Joule} became quite enhanced and varied between 90 and 50 W/kg (see Figures 4f–4j). Oppositely, during Period 1 when the polar TOI was absent, central polar Q_{Joule} values became significantly smaller (≤20 W/kg; see Figures 3a–3e and 4a–4e).

Continuing with the 0–180°E sector, Joule heating reached its Northern Hemisphere maximum in the auroral zone. According to the maximum values indicated by the maps' color scales, the maximum auroral Q_{Joule} values were higher during Period 2 than Period 1. Furthermore, the maximum auroral values are significantly larger than the polar values inside the polar cap and over the magnetic pole.

3.4. Precipitation Void in the Vicinity of Polar TOI on the Nightside in Period 2

Figure 5 is constructed with multiinstrument data for the Northern Hemisphere in order to investigate the various aspects of SED-TOI structure appearing over North America at ~2040 UT in Period 2. In Figure 5a, the relevant TIE-GCM Q_{Joule} line plot (at 80°N; 350 km altitude) and Northern Hemisphere map (at 2040 UT) are displayed. In the 180–360°E sector of our interest, the Q_{Joule} line plot illustrates a well-defined Q_{Joule} enhancement over the magnetic pole. This is further illustrated with the Q_{Joule} map depicting a well-defined Q_{Joule} enhancement over the magnetic pole with some areas of high and minimum Joule heating rates in the polar cap and with some bands of high Q_{Joule} in the vicinity of the auroral zone. We note also that in the 0–180°E sector, the Q_{Joule} line plot tracked a broader aurora-related peak centered over 150°E, as the auroral zone positioned at higher geographic latitudes. This is further illustrated with the Q_{Joule} map tracking high to maximum values at auroral latitudes.

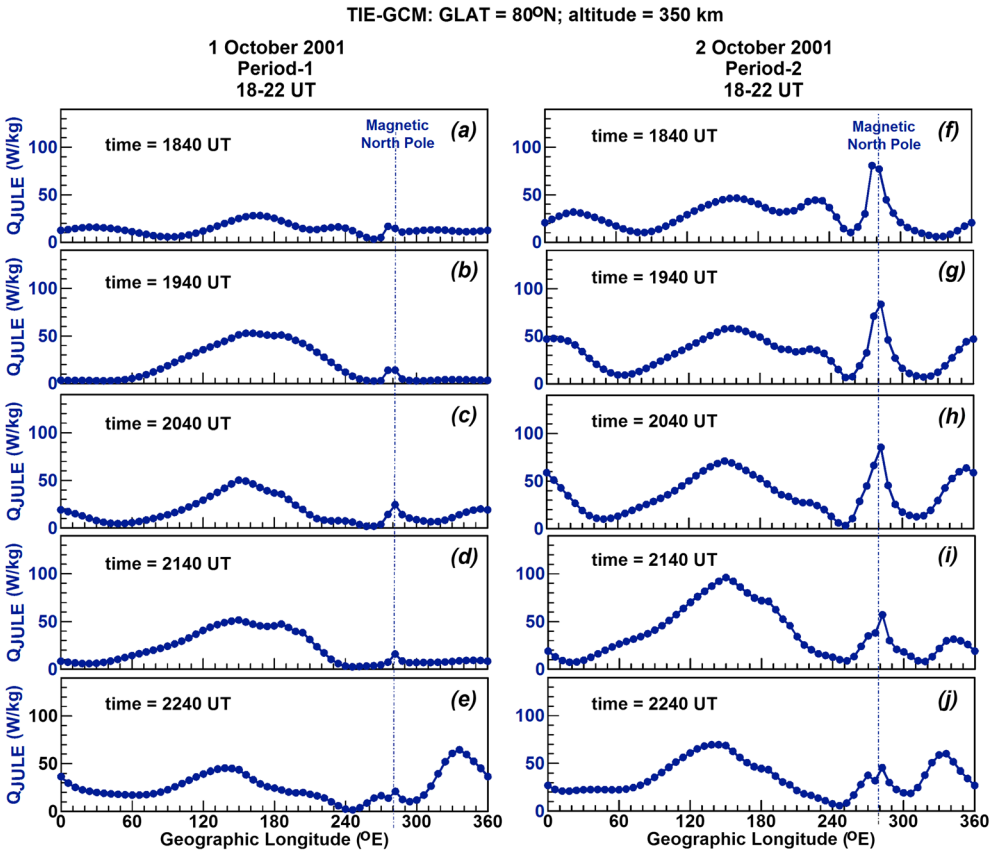

Figure 4. The Q_{Joule} line plots sets are constructed for 80°N (geographic) latitude passing through the magnetic North Pole at 280°E and for the GPS TEC maps shown in Figure 2 and TIE-GCM Q_{Joule} maps shown in Figure 3. Over the magnetic pole (a–e) there is only a small Joule heat intensification when the polar TOI was absent, while (f–j) a large and well-defined peak is evident when the polar TOI was present.

In Figure 5b, the Northern Hemisphere map illustrates the geographic configuration of magnetic meridians, the geographic position of magnetic pole, and the ground track of spacecraft F13, while 80°N is also marked. The auroral oval's poleward and equatorward boundaries plus the magnetic dip equator are also plotted. The trough and polar TOI positions tracked by spacecraft F13 are also marked (see details below). In order to obtain a polar cross section, we utilized an ascending pass and a small section of the following descending pass. Therefore, the position of spacecraft turning is also marked (indicated as arrow in cyan). As the ground track reveals, this pass progressed over the magnetic pole. Covering the 30 min time period of 2002–2032 UT, the regional (in Figure 5b) and polar (in Figure 5c) TEC maps depict the northern ionosphere. We note here that the EIA is not well visible because of the patchy data coverage and therefore is not labeled. In the American sector, a SED plume (59–70 TECU; indicated in green) passed through the dayside cusp over central North America. After entering the polar region, the SED plume propagated over the magnetic pole and into the nightside and formed a polar TOI (35–47 and 23–35 TECU; indicated as green and yellow, respectively).

Overall, Figures 5a–5c provide observational and theoretical evidence that in the American sector, the local Q_{Joule} increase (~80 W/kg) over the magnetic pole was associated with the polar TOI. Over North America, auroral Q_{Joule} values were sometimes lower than and sometimes comparable to the polar Q_{Joule} values. These imply that the polar TOI was associated with Joule heating intensification in the magnetic pole's vicinity where energy deposition occurred due to the configuration of IEF $\mathbf{E_Y}$ and the increased magnitudes of $\mathbf{E_M}$ and $\mathbf{E_P}$ (see Figures 1f and 1g).

For further investigating this polar TOI, we have utilized a set of F13 data. These are presented as spectrogram image (see Figure 5d) and line plots (see Figure 5e). F13 crossed the polar region and the magnetic pole (see also spacecraft ground track in Figure 5b). In Figure 5d, the electron spectrogram image is shown,

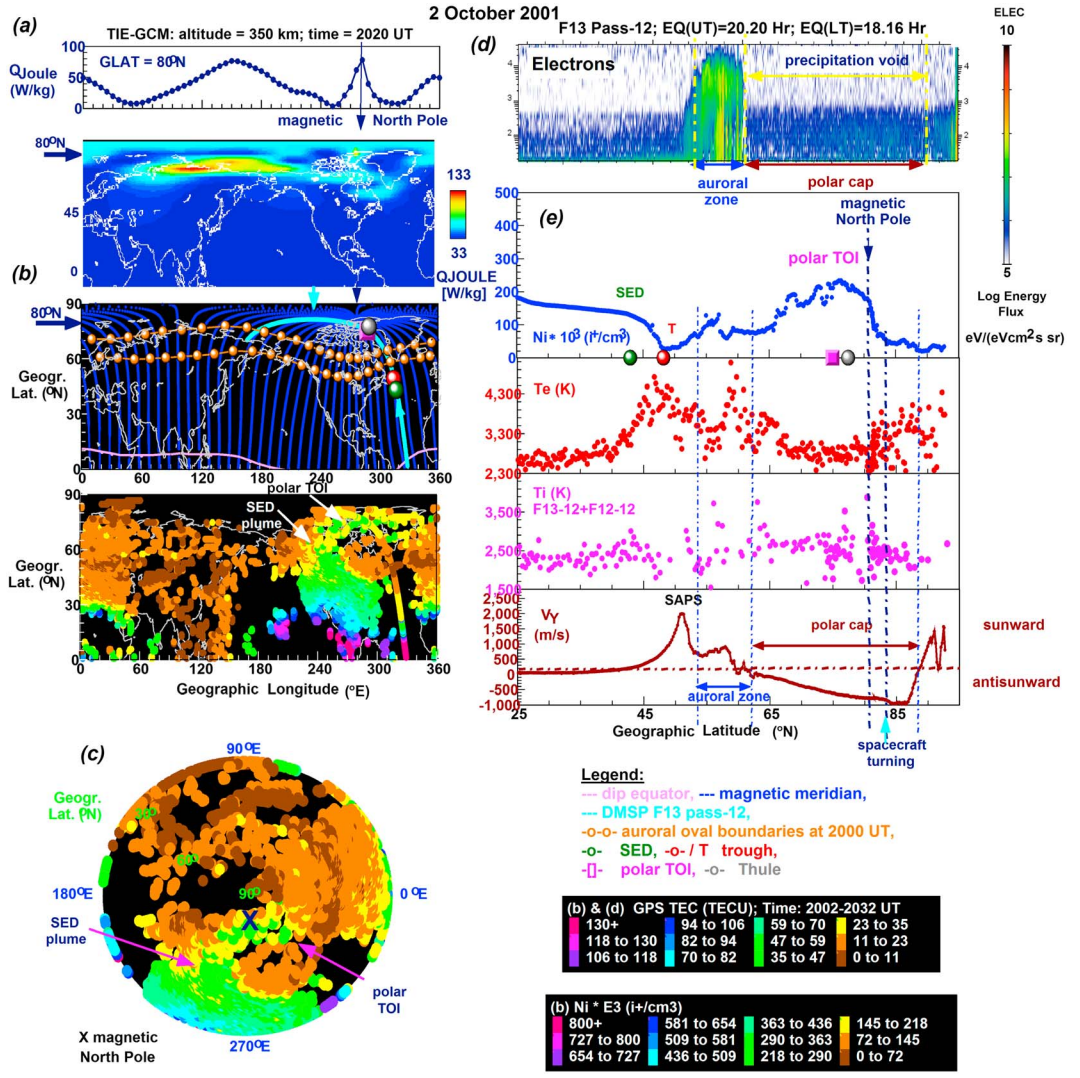

Figure 5. The various aspects SED plume-polar TOI structure appearing in the American sector on 2 October 2001 at ~20 UT during Period 2 is illustrated with a set of plots. These are (a) the TIE-GCM Q_{Joule} line plot and map; (b) the northern map illustrating the auroral oval boundaries, magnetic dip equator, ground track of F13 providing topside measurements, and regional GPS TEC map where the Ni data are also plotted; (c) the polar GPS TEC map; (d) the spectrogram image depicting that the polar TOI occurred with precipitation void on the nightside; and (e) the multiinstrument F13 line plot sets. In the spectrogram image, the E flux is measured in [eV/(eV cm^2 s sr)], where sr is steradian or square radian defined as (radius)^2.

and the regions of auroral zone and polar cap are marked based on the classification of *Newell et al.* [1996]. Some strong and structured electron precipitations can be seen in the auroral zone. Some weak precipitation classified as void is apparent in the polar cap. Although the polar TOI tends to occur with polar rain, the polar rain has a strong noon-midnight gradient along which polar rain electrons steadily decline from dayside to nightside in the ionosphere [*Torbert et al.*, 1981]. Possibly, the noon-midnight gradient caused the occurrence of precipitation void in the local nighttime sector of this scenario. Furthermore, the presence of void can also indicate open field lines and dayside reconnection [*Sotirelis et al.*, 1997].

In Figure 5e, the Ni plot depicts a small SED on the trough's equatorward edge, a small section of the auroral zone, some plasma depletions in the polar cap region, and the cross section of the polar TOI appearing as a well-defined plasma density enhancement (260×10^3 (i$^+$/cm^3)). By adding these Ni data to the TEC map (see Figure 5b), their good match is obvious and provides evidence that the polar TOI was tracked by the Ni line plot. Meanwhile, the Te and Ti line plots depict some important thermal characteristics. These are the subauroral Te peak (5000 K), which is created by frictional heating and defines the coinciding

locations of trough minimum and plasmapause [*Prolss*, 2006], and the significantly lower electron temperatures at midlatitudes (2300 K) and in the polar cap region (2800 K) that are due to the cold SED plume plasma convected from subauroral latitudes [*Foster et al.*, 2002]. We note here that because of the incomplete F13 Ti data coverage, we added F12 Ti data (from a similar pass) to the Ti line plot. As shown, Ti peaked at ~3500 K in the auroral zone, close to the auroral/polar cap boundary, close to Thule where the polar TOI became best developed, and over the magnetic pole. The detection of Ti peaks at auroral and polar latitudes could imply multiple Joule heating locations as Joule heating energizes ions via friction or collision. These Ti peaks support also the validity of TIE-GCM-modeled auroral and polar Q_{Joule} increases implying also local Joule heating intensifications (see details in section 5). Finally, the V_Y line plot tracked the signature of SAPS **E** field appearing as a maximized sunward (+) drift that reached ~2300 m/s. A strong SAPS **E** field (see also Figure 1i) is crucial for both SED plume plasma development plus sunward and poleward SED plume plasma transport [*Foster et al.*, 2002]. In the polar cap, the antisunward (−) plasma drift reached ~−800 m/s at polar TOI latitudes providing evidence of the SED plume plasma's convective horizontal plasma transport by antisunward drift.

Overall, these DMSP F13 observations, obtained close to the magnetic pole, demonstrate that the polar TOI was accompanied with precipitation void in the local evening-nighttime sector providing evidence of dayside merging. Some isolated Ti peaks demonstrate multiple Joule heating locations at auroral and polar latitudes and close to the magnetic pole. These results imply that the thermosphere could be energized in the central polar cap as *Huang et al*. [2014a] pointed out and when the polar TOI is present during dayside merging as our results demonstrate.

3.5. Polar Rain in the Vicinity of Polar TOI on the Dayside in Period 2

Figure 6 is constructed in a similar fashion as Figure 5 allowing comparisons and shows that the polar TOI was still well developed at the end of Period 2 at ~2330 UT.

Figure 6a shows the TIE-GCM-simulated Q_{Joule} line plot (80°N; 350 km altitude) and map. We focus on the 180–360°E sector that depicts multiple Q_{Joule} intensifications. Along 80°N, the Q_{Joule} line plot tracked a smaller peak close to the magnetic pole (270°E, ~50 W/kg) and a larger peak over Greenland (330°E, ~70 W/kg). Meanwhile, the Q_{Joule} map depicts local intensifications both in the polar cap and in the auroral zone. In Figure 6b, the top map depicts the ground track of spacecraft F13 with the magnetic meridians and the auroral oval boundaries. The locations of SED, trough, and polar TOI tracked by spacecraft F13 are also indicated. As the spacecraft ground track reveals, this pass did not progress over the magnetic pole. Both the regional (in Figure 6b) and the polar (in Figure 6c) TEC maps show that the SED plume and the polar TOI were less developed than earlier (see Figure 5). The regional TEC map shows also the matching Ni data provided by spacecraft F13. Together, these TEC and Ni data illustrate that spacecraft F13 tracked a small section of the polar cap and a cross section of the polar TOI close to but not over the magnetic pole.

In Figure 6d, the electron spectrogram image is shown, and the regions of auroral zone and polar cap are marked. Some strong and structured electron precipitations can be seen in the boundary plasma sheet associated with the discrete aurora [*Newell et al.*, 1996]. Some more homogeneous precipitations are apparent in the central plasma sheet associated with the diffuse aurora [*Newell et al.*, 1996]. Homogeneous precipitations of a few hundreds of eV electrons continued across the dayside polar cap as polar rain [*Winningham and Heikkila*, 1974] during the local afternoon-midday hours in line with the noon-midnight gradient. On the dayside, polar rain tends to occur with the polar TOI and during dayside reconnection and thus indicates open field lines [*Sotirelis et al.*, 1997]. During dayside reconnection ($\mathbf{B_Z} \approx -8$ nT), solar particles have direct access to the polar magnetosphere and ionosphere. When the merging rate is high, as implied by the high cross PCP drop ($\Phi_{PC} \approx 170$ kV), open field lines are rapidly dragged across the polar cap antisunward [*Dungey*, 1961] (i.e., in the vicinity of polar TOI during this scenario) and thus solar particles can reach the ionosphere.

In Figure 6e, the matching line plots are illustrated, while the auroral zone and polar cap are also marked. To describe them, the Ni line plot tracked the feature of SED on the trough's equatorward edge, a narrow section of the auroral zone, and the low-density background plasma in the polar cap with a large polar TOI. Meanwhile, the Te line plot tracked the subauroral Te peak (~4400 K) marking the trough location. Some low Te (~2400 K) underlying the polar TOI verifies that the cold SED plume plasma became convected into the polar cap by antisunward convection, as evidenced by the V_Y line plot. Although the Ti data are sporadic

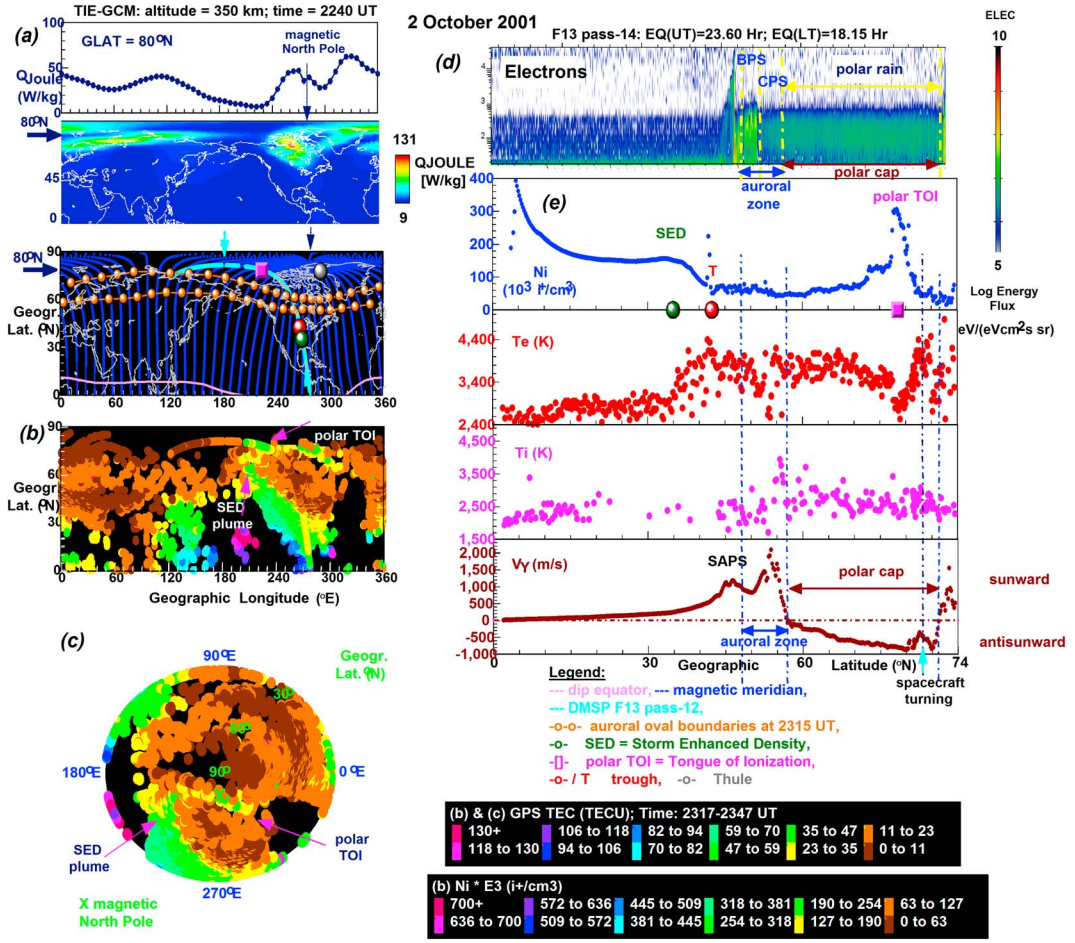

Figure 6. Similar to Figure 5 but for a SED plume-polar TOI structure appearing over North America at the end of Period 2 when the polar TOI occurred with polar rain on the dayside.

at midlatitudes, the high values close to the aurora/polar cap boundary (~4000 K) plus the slightly lower values in the polar cap (~3500 K) and at polar TOI latitudes (~3000 K) are clearly visible. These elevated Ti values imply (1) magnetospheric energy dissipation by Joule heating and (2) multiple Joule heating locations in the ionosphere since Joule heating energizes ions via friction or collision. Meanwhile, the V_Y line plot tracked the SAPS **E** field signature (~1200 m/s; see also Figure 1i) and some strong auroral sunward drifts (~2000 m/s). Large antisunward drifts, reaching ~−900 m/s at polar TOI latitudes, provided transpolar plasma transport for the SED plume plasma.

Overall, these observations are obtained away from the magnetic pole and demonstrate that there was dayside merging, as evidenced by polar rain, in the vicinity of polar TOI during the local afternoon-midday hours. In the polar cap Ti was mostly ~3000 K but some peaks reaching ~3500 K also occurred. These elevated Ti values imply that the thermosphere could be energized at polar latitudes as *Huang et al*. [2014a] pointed out and when the polar TOI is present during the process of dayside merging as our results demonstrate.

3.6. Precipitation Void in the Absence of Polar TOI During Period 1

Figure 7 is constructed for ~1940 UT in Period 1 when the polar TOI was absent. We note here that because of the incomplete F13 Ti data coverage, we added F15 Ti data—showing a similar trend—to the Ti line plot. Furthermore, due to the lack of OVATION data, we have plotted the Heppner-Maynard Boundary (HMB) to get an indication of the polar convection's latitudinal extent [*Heppner and Maynard*, 1987].

Figure 7a illustrates the TIE-GCM-simulated Q_{Joule} line plot (80°N; 350 km altitude) and map for this scenario. In the 180–360°E sector of our interest, the line plot tracked a minor Q_{Joule} peak (~20 W/kg) over the magnetic

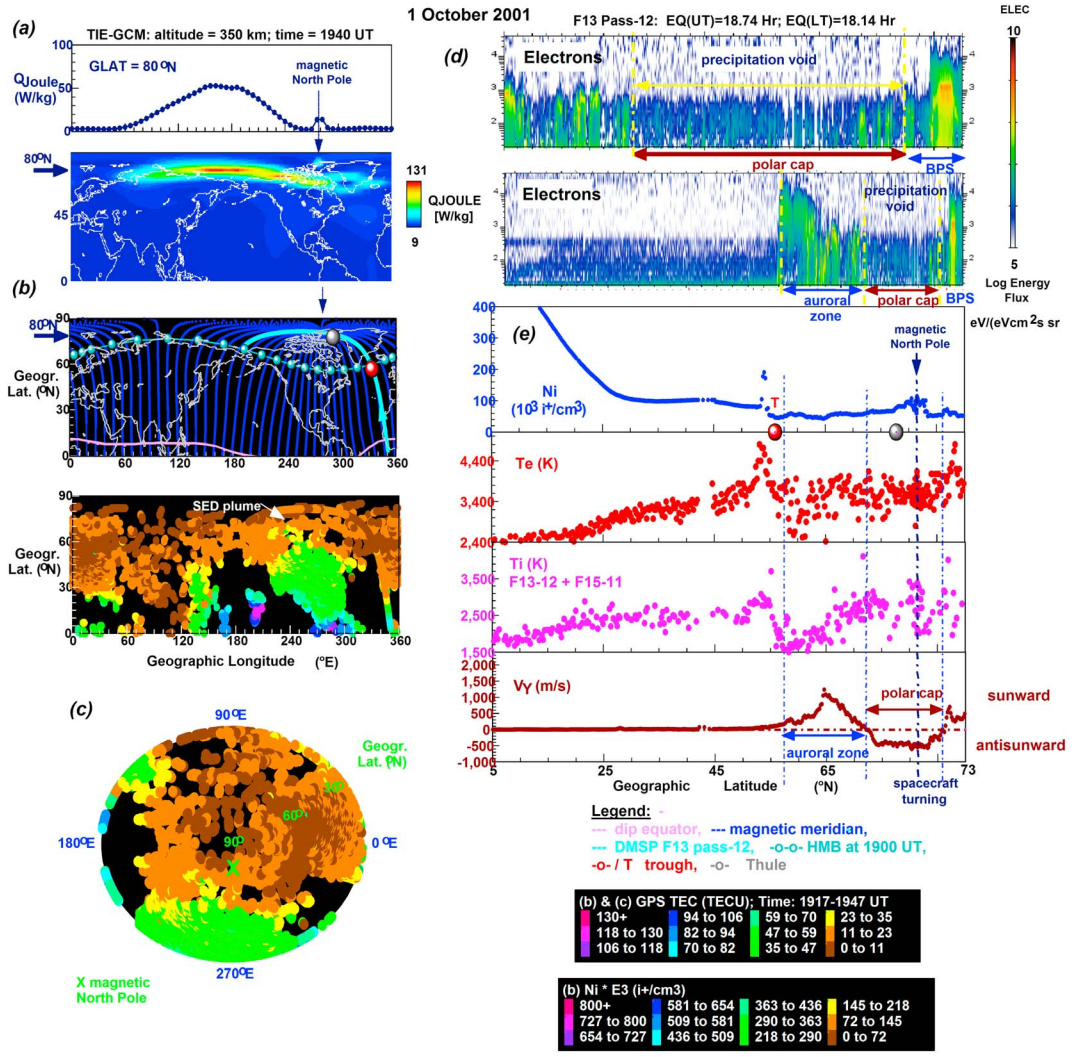

Figure 7. Similar to Figure 5 but for a SED plume appearing without a polar TOI over North America during Period 1 in the absence of polar rain.

pole and in the polar TOI's absence. The Q_{Joule} map shows an isolated patch of minor intensification and a band of high to maximum intensification in the auroral zone. In the 0–180°E sector, the line plot tracked some high values (60 W/kg). Meanwhile, the Q_{Joule} map shows that these high values are related to the high Q_{Joule} band of the auroral zone situated at high geographic latitudes.

In Figure 7b, the top map illustrates that the F13 pass employed was aligned with the magnetic meridian, passed over the magnetic pole, and covered the entire polar cap region in the Western Hemisphere. Meanwhile, the TEC map tracked over the North American continent a SED plume that propagated across the dayside cusp but did not enter the polar cap. This is also shown in the polar TEC map (see Figure 7c). Thus, there was no polar TOI development and the entire polar cap became a region of low TEC (0–11 and 11–23 TECU; indicated in dark brown and orange, respectively). This regional TEC map illustrates also the matching Ni data from the F13 pass crossing this low TEC region over North America and the magnetic pole.

In Figure 7d, the matching electron spectrogram image is shown (see bottom image) with a more detailed section of the polar cap (see top image). In both spectrogram images, the regions of auroral zone and polar cap are marked. The lack of homogeneous precipitation or polar rain in the polar cap is apparent and is marked as precipitation void after *Newell et al.* [1996]. Precipitation void was detected on the nightside. In accordance with the observational results shown in Figures 1f–1h, we speculate that this dropout of polar

rain was due to the combined effects of slow merging rate ($\Phi_{PC} \approx 40$ kV) [*Sotirelis et al.*, 1997] and existing noon-midnight polar rain gradient [*Torbert et al.*, 1981] (see details in section 5).

In Figure 7e, the Ni line plot tracked the trough of which location is marked by the subauroral Te peak, the low plasma densities in the polar cap, and a minor Ni increase over the magnetic pole. Due to the absence of cold SED plume plasma in the polar cap, Te remained as high as in the auroral zone (~3000 K). Ti data from F13 and F15 (see details above) depict increasing values (from 1500 to 3300 K) in the auroral zone and a well-defined increase (from 2000 to 3600 K) over the magnetic pole suggesting Joule heating locations at the auroral/polar cap boundary and at the magnetic pole, respectively. Although with some possible underestimations, the polar enhancement can be seen in the TIE-GCM-simulated Q_{Joule} data (see Figure 7a). As the V_Y line plot illustrates, the SAPS **E** field was absent but the auroral sunward convection was strong (~1000 m/s) and the antisunward convection was evenly ~−500 m/s.

Overall, these observations suggest that there was no polar TOI development due to the weak IEF $\mathbf{E_Y}$, weak geo-effective $\mathbf{E_M}$, and consequential weak polar **E** field ($\mathbf{E_P}$) and horizontal polar convection (Φ_{PC}) (see Figures 1e and 1h). Caused by the combined effects of weak dayside reconnection and noon-midnight polar rain gradient, precipitation void was present on the nightside.

4. Analyzing U_{SW} Transfer to the Coupled M-I System

Figure 8 illustrates a set of time series depicting some important aspects of IMF orientation and energetics characterizing the days of 1 and 2 October 2001. Aiding our analysis, the intervals of Period 1 and Period 2 are highlighted. Figures 8a and 8b show the orientations of IMF $\mathbf{B_Z}$ and $\mathbf{B_Y}$ components (nT). Southward $\mathbf{B_Z}$ decreased from −6 to 0 nT during Period 1 and remained close to −8 nT during Period 2. This long-lasting southward $\mathbf{B_Z}$ orientation implies long-lasting dayside reconnections facilitating solar wind energy deposition into the magnetosphere [*Dungey*, 1961]. While $\mathbf{B_Y}$'s polarity changed frequently during Period 1, $\mathbf{B_Y}$ remained negative during Period 2. Due to the nonzero $\mathbf{B_Y}$ and its variability, polar convection had varied and had been asymmetric about the noon-midnight meridian [*Dungey*, 1961].

Figures 8c–8f illustrate the time series of solar wind energy available (U_{SW}; TW, where $T = 10^{12}$), geo-effective or merging **E** field ($\mathbf{E_M}$; mV/m), efficiency of energy input (EI_{eff}; %) from the solar wind to the magnetosphere, and energy transferred from the solar wind to the magnetosphere (U_ε; TW). As expected, there is a close correlation among $\mathbf{E_M}$, EI_{eff}, and U_ε. Describing Periods 1 and 2, $\mathbf{E_M}$, EI_{eff}, and U_ε attained minimal values during Period 1 and high values during Period 2. Meanwhile, U_{SW} varied oppositely exhibiting high values in Period 1 and minimal values in Period 2. All these variations imply that U_{SW} does not directly drive the resultant electrodynamic processes taking place in the magnetosphere [*Lu et al.*, 1998]. It is rather the efficiency of solar wind energy transfer to the magnetosphere (i.e. EI_{eff})—depending on the magnetosphere's geo-effectiveness or $\mathbf{E_M}$ [*Li et al.*, 2012] and also on U_ε—that matters than the U_{SW} available [*Lu et al.*, 1998]. EI_{eff} decreased gradually to close to zero and then increased back to ~0.15% during Period 1 when the polar TOI was absent. Oppositely, EI_{eff} oscillated and reached higher values (~1.5%) during Period 2 when the polar TOI appeared. We speculate that these results show only some necessary conditions for the polar TOI to be absent or present, but not the sufficient conditions. For example, *Liu et al.* [2015] reported opposite scenarios when the polar TOI was absent under stronger southward $\mathbf{B_Z}$ and was present when southward $\mathbf{B_Z}$ was weaker. We note also that even the 1.5% appears to be a small value, these percent values are in good agreement with the recent statistical results of *Li et al.* [2012] reporting ~2.8% for a medium intensity storm and ~1.9% for the following recovery phase.

5. Discussions

First, we discuss our TIE-GCM-generated Joule heating rate (Q_{Joule}) results. These provide information on the variations of both Joule heating and Ti [*Fujiwara et al.*, 2007]. Although TIE-GCM Joule heating data show good correlations with satellite measurements [*Deng et al.*, 2008], it is possible that the model values are underestimated [*Huang et al.*, 2014a, 2014b]. Regarding the spatial distribution of Q_{Joule} at high latitudes (see Figures 3 and 4), the Q_{Joule} line plots and maps demonstrate multiple energy depositions in the auroral zone and polar cap region. Over the magnetic pole, a well-defined Q_{Joule} peak occurred that decreased from ~80 to ~40 W/kg during Period 2 and a small Q_{Joule} peak (~20 W/kg) appeared during Period 1. Our results

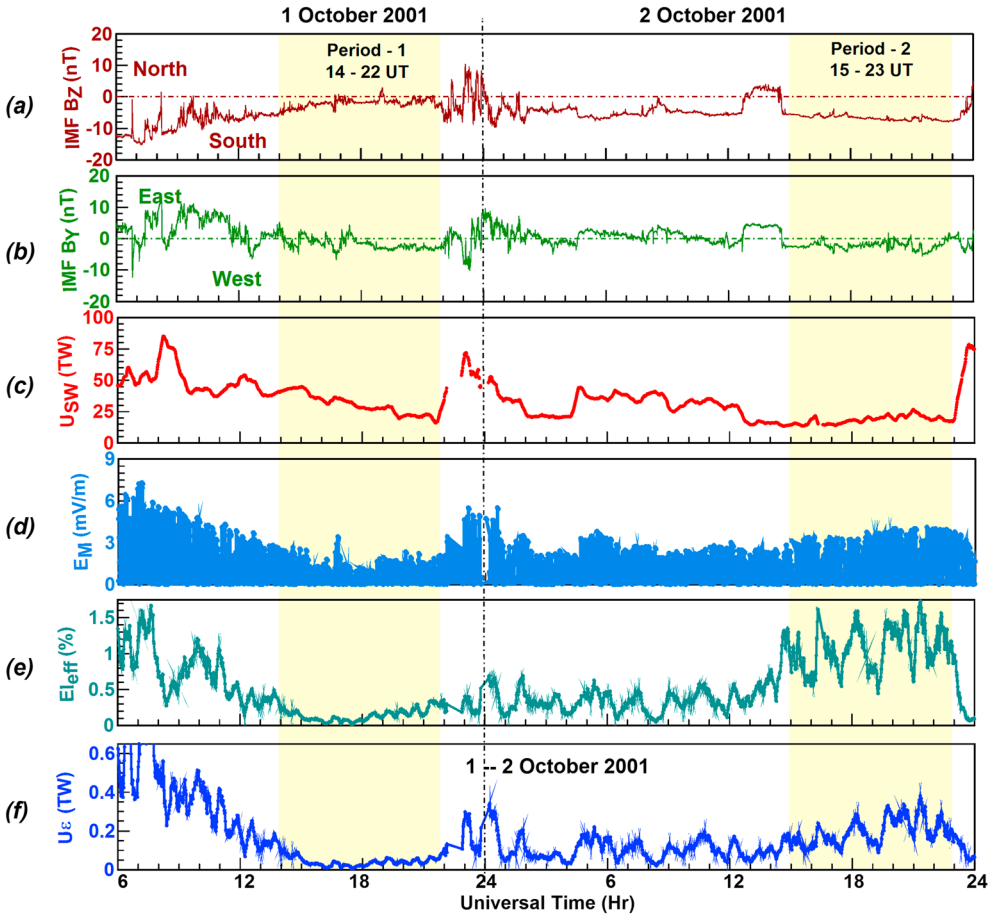

Figure 8. A small collection of line plot series illustrates (a, b) the IMF $\mathbf{B_Z}$ and $\mathbf{B_Y}$ components and (c–f) the temporary variation of storm time energetics plus the time intervals chosen for highlighting differences. Particularly during Periods 1 and 2, the (Figure 8c) solar wind energy available (U_{SW}) varied oppositely with the (Figure 8d) merging or geo-effective **E** field ($\mathbf{E_M}$), (Figure 8e) energy input efficiency (El_{eff}), and (Figure 8f) energy deposited into the magnetosphere (U_{ε}). Their opposite phase during Periods 1 and 2 are apparent.

obtained with various data imply that the central polar cap region is one of the preferred places of (1) energy deposition facilitated by $\mathbf{E_M}$ and $\mathbf{E_P}$, (2) Joule heating intensification, and (3) Ti increase. Recently, *Huang et al.* [2014a, 2014b] pointed out that the common centers of primary energy deposition and Joule heating are located at ~83°N (magnetic), close to the magnetic pole. With our $\mathbf{E_M}$ and $\mathbf{E_P}$ results, demonstrating the intensity of magnetic merging over the magnetic pole, we add to their studies and thus further demonstrate the significance of central polar cap in energy deposition. Our reasoning is that the merging **E** field is a parameter related to the energy input from the solar wind to the magnetosphere taking place in the polar cap where the magnetic field lines are open [*Kan and Lee*, 1979]. Furthermore, $\mathbf{E_M}$ is equivalent with the dimensionless polar cap or PC index (PC = $\mathbf{E_M}$) [*Stauning*, 2007] that can be derived from magnetometer data from Thule (87.68°N), situated near the magnetic pole (see Figure 5e). This equality implies also, in an independent way, some significant energy deposition taking place close to or over the magnetic pole that is facilitated by $\mathbf{E_M}$ in the magnetosphere and by its mapped-down ionospheric equivalent, $\mathbf{E_P}$, in the ionosphere. Therefore, there is a close correlation between Q_{Joule} and $\mathbf{E_M}$-$\mathbf{E_P}$ in the central polar cap.

Next, we discuss (i) the SED-TOI and SED structures' close correlation with the above-discussed Q_{Joule}-$\mathbf{E_M}$-$\mathbf{E_P}$ variations and (ii) the impact of Joule heating on the polar TOI. (i) Solar wind-produced $\mathbf{E_M}$ controls both the coupled SW-M-I system and the horizontal polar convection. Thus, under intensive (or weak) Q_{Joule}-$\mathbf{E_M}$-$\mathbf{E_P}$ conditions, polar convection is strong (or weak). Strong polar convection is crucial for polar TOI development like in Period 2, and weaker polar convection leads to SED development only [*Foster et al.*, 2005] like in

Period 1. (ii) Since $\mathbf{E_M}$ maps down the magnetic field lines to the ionosphere's central polar cap region as $\mathbf{E_P}$, the electromagnetic energy deposited dissipates as resistive Joule heating and generates multiple Joule heating enhancements and Ti intensifications by energizing ions (see Figure 1j). Energized ions interact with neutrals via friction or collision depending on the relative ion and neutral densities and lead to Ti increases [*Huang et al*., 2014a]. As our results demonstrate, the polar TOI developed under intensive Q_{Joule}-$\mathbf{E_M}$-$\mathbf{E_P}$ conditions (i.e., Period 2) and was accompanied by Q_{Joule} and Ti enhancements in the central polar cap region. Oppositely, there was no polar TOI under weak Q_{Joule}-$\mathbf{E_M}$-$\mathbf{E_P}$ conditions (i.e., Period 1) when smaller Q_{Joule} intensifications occurred over the magnetic pole. Although the main energy source of resistive Joule heating is $\mathbf{E_M}$, the variability of ionospheric polar **E** field, neutral winds, and electron densities can also vary both the amount of Joule heating generated and the resultant ion temperature produced via feedback mechanisms [*Deng and Ridley*, 2006a]. Since we could not isolate the individual Joule heating components (i.e., Joule heating generated by (i) $\mathbf{E_M}$ and (ii) feedback mechanisms), only their net effects could be observed in the Q_{Joule} and Ti data. As we observed, even the highest Ti in the polar cap remained under 4000 K. We know from modeling studies (see details in section 1) that Joule heating-related upward drift increases plasma density in the topside ionosphere [*Deng and Ridley*, 2006b], and Ti under 4000 K does not erode the polar TOI [*Valladares et al*., 1998]. Therefore, we speculate that both the Joule heat-related upward motion and the lower (than 4000 K) Ti contributed to the well development and maintenance of polar TOI by keeping the SED plume plasma at greater heights of lower recombination rates and by not reducing significantly the SED plume plasma's O^+ content.

Finally, we discuss dayside merging occurring at different rates that was evidenced by polar rain and precipitation void. As demonstrated by a scenario in Period 2 (see Figure 6), strong dayside reconnection ($\mathbf{B_Z} \approx -8$ nT) and strong dayside merging ($\mathbf{E_M} \approx 5$ mV/m) occurring at high merging rate ($\Phi_{\text{PC}} \approx 170$ kV) imply intensive transport of energy flux and SED plume plasma across the polar cap [*Sotirelis et al*., 1997]. Under such conditions, the polar TOI tends to appear with polar rain. The reason is that when the merging rate is high, then the high- and low-altitude ends of newly open field lines move quickly across the polar cap. This field line configuration allows suprathermal solar wind electrons reach the ionosphere [*Sotirelis et al*., 1997] appearing as polar rain on auroral imagery. As an opposite scenario in Period 2 (see Figure 5), our results demonstrate also the occurrence of polar TOI with precipitation void on the nightside during strong dayside reconnection ($\mathbf{B_Z} \approx -8$ nT) and strong dayside merging ($\mathbf{E_M} \approx 5$ mV/m; $\Phi_{\text{PC}} \approx 140$ kV). This scenario can be explained with the polar rain's strong noon-midnight gradient along which polar rain electrons rapidly decline from the dayside to the nightside. During the local evening hours of such an intense merging event, the SED plume plasma evolved into a polar TOI but the polar rain electrons decreased to levels that are classified as void. Our results show also another opposite scenario of weak dayside merging during Period 1 leading to the development of a low plasma density polar cap region and precipitation void (see Figure 7) during dayside reconnection. Period 1 was a time interval of small southward $\mathbf{B_Z}$ (~-2 nT), low $\mathbf{E_M}$ (~2.5 mV/m), and small Φ_{PC} (~40 kV). These parameters imply dayside reconnection occurring at low merging rate and weak plasma transport across the polar cap. Under such conditions, the SED plume plasma could not propagate across the polar cap and thus inhibited the development of polar TOI and therefore left the polar cap a region of low plasma density. Furthermore, at low merging rate ($\Phi_{\text{PC}} \approx 40$ kV), newly open field lines are highly stressed since their high- and low-altitude ends are farther apart. While the low-altitude end is still sunward, the high-altitude end is already tailward because the next merging event is being still awaited due to the slow merging process. Such stressed field line configuration minimizes the entering of suprathermal solar wind electrons and thus leads to polar rain-like precipitation with very low energy fluxes that are classified as void [*Sotirelis et al*., 1997].

6. Conclusions

We have investigated the North American sector for its ionospheric response to the 1–2 October 2001 geomagnetic events. We have analyzed SW-M-I coupling processes taking place during SED scenarios in Period 1 when the energy input efficiency (EI_{eff}) was low and during SED-TOI scenarios in Period 2 when the energy input efficiency (EI_{eff}) was higher. These scenarios commonly occurred during dayside reconnection ($\mathbf{B_Z} < 0$) and dayside merging (1.5 mV/m $< \mathbf{E_M} <$ 5 mV/m) occurring at various rates (30 kV $< \Phi_{\text{PC}} <$ 140 kV). Based on multiinstrument observational and theoretical TIE-GCM Q_{Joule} results, our important findings

obtained for Periods 1 and 2 are as follows. According to the spatial distribution of Q_{Joule} and latitudinal variation of Ti, energy deposition occurred at multiple points and the magnetic North Pole appeared to be one of the preferred places. In the central polar cap, Q_{Joule} and Ti intensified significantly (or moderately) in the presence (or absence) of polar TOI. Dayside merging taking place in the polar cap was confirmed by the detection of polar rain or precipitation void, depending on both the orientation of noon-midnight gradient and the intensity of merging rate monitored with Φ_{PC}. The intensity of dayside merging in the central polar cap was monitored with the magnetospheric merging **E** field ($\mathbf{E_M}$) and with its mapped-down ionospheric equivalent, $\mathbf{E_P}$. These showed a similar trend as the polar TOI was present (or absent) under high (or low) Φ_{PC}-$\mathbf{E_M}$-$\mathbf{E_P}$ conditions. Under these varying energy deposition conditions, the underlying feedback and coupling mechanisms could contribute to the close interconnection between the enhanced (or moderate) Joule heat and Ti intensifications in the presence (or absence) of polar TOI. Since Ti intensifications occurred below 4000 K, possibly the below 4000 K Ti along the resultant upward motion of the F_2 layer contributed to the development and maintenance of polar TOI by keeping the SED plume plasma at greater heights of low recombination rates and by not increasing O^+ recombination rates and therefore not eroding the polar TOI. From these results obtained for Periods 1 and 2, we conclude that (1) EI_{eff} could be used as a diagnostic of the intensity of polar TOI and (2) the thermosphere might be intensively (or moderately) impacted during dayside merging when the polar TOI is present (or absent).

Acknowledgments

This material is based on research sponsored by the Air Force Research Laboratory, under agreement FA2386-15-1-4043. The U.S. Government is authorized to reproduce and distribute reprints for Governmental purposes notwithstanding any copyright notation thereon. We are grateful to the ACE SWEPAM instrument team, the ACE Science Center, for providing the ACE data. We gratefully acknowledge the Center for Space Sciences at the University of Texas at Dallas and the U.S. Air Force for providing the DMSP thermal plasma data. We also thank the World Data Center for Geomagnetism at Kyoto [http://wdc.kugi.kyoto-u.ac.jp/wdc/Sec3.html] for providing the geomagnetic data and indices and the Space Physics Interactive Data Resource (SPIDR) for the magnetic data [http://spidr.ngdc.noaa.gov/spidr/dataset.do?view=geomagnetic]. Special thanks are extended to MIT for the GPS TEC data in the Madrigal Database. We are thankful to Virginia Tech for the Interactive Map Potential Plotting tool (http://vt.superdarn.org/tiki-index.php?page=DaViT+Map+Potential+Plot) and to the Community Coordinated Modeling Center at NASA Goddard Space Flight Center for the TIE-GCM model simulations. Simulation results have been provided by the Community Coordinated Modeling Center through their public Runs on Request system (http://ccmc.gsfc.nasa.gov). The CCMC is a multiagency partnership between NASA, AFMC, AFOSR, AFRL, AFWA, NOAA, NSF, and ONR. The TIE-GCM was developed by Roble et al. at the High Altitude Observatory (HAO), National Center for Atmospheric Research (NCAR).

References

Akasofu, S. I. (1981), Energy coupling between the solar wind and the magnetosphere, *Space Sci. Rev.*, *28*(2), 121–190, doi:10.1007/BF00218810.

Anderson, P. C., D. L. Carpenter, K. Tsuruda, T. Mukai, and F. J. Rich (2001), Multisatellite observations of rapid subauroral ion drifts (SAID), *J. Geophys. Res.*, *106*(A12), 29,585–29,599, doi:10.1029/2001JA000128.

Blanc, M., and A. Richmond (1980), The ionospheric disturbance dynamo, *J. Geophys. Res.*, *85*(A4), 1669–1686, doi:10.1029/JA085iA04p01669.

Boyle, C. B., P. H. Reiff, and M. R. Hairston (1997), Empirical polar cap potentials, *J. Geophys. Res.*, *102*(A1), 111–125, doi:10.1029/96JA01742.

Carpenter, D. L., and J. Lemaire (2004), The plasmasphere boundary layer, *Ann. Geophys.*, *22*, 4291–4298, doi:10.5194/angeo-22-4291-2004.

Chappell, C. R. (1972), Recent satellite measurements of the morphology and dynamics of the plasmasphere, *Rev. Geophys.*, *10*(4), 951–979, doi:10.1029/RG010i004p00951.

Chappell, C. R. (1974), Detached plasma regions in the magnetosphere, *J. Geophys. Res.*, *79*(13), 1861–1870, doi:10.1029/JA079i013p01861.

Codrescu, M. V., T. J. Fuller-Rowell, and J. C. Foster (1995), On the importance of E-field variability for Joule heating in the high-latitude thermosphere, *Geophys. Res. Lett.*, *22*, 2393–2396, doi:10.1029/95GL01909.

Deng, Y., and A. J. Ridley (2006a), Role of vertical ion convection in the high-latitude ionospheric plasma distribution, *J. Geophys. Res.*, *111*, A09314, doi:10.1029/2006JA011637.

Deng, Y., and A. J. Ridley (2006b), Dependence of neutral winds on convection E-field, solar EUV, and auroral particle precipitation at high latitudes, *J. Geophys. Res.*, *111*, A09306, doi:10.1029/2005JA011368.

Deng, Y., and A. J. Ridley (2007), Possible reasons for underestimating Joule heating in global models: *E* field variability, spatial resolution, and vertical velocity, *J. Geophys. Res.*, *112*, A09308, doi:10.1029/2006JA012006.

Deng, Y., A. Maute, A. D. Richmond, and R. G. Roble (2008), Analysis of thermospheric response to magnetospheric inputs, *J. Geophys. Res.*, *113*, A04301, doi:10.1029/2007JA012840.

Dungey, J. W. (1961), Interplanetary magnetic field and the auroral zones, *Phys. Rev. Lett.*, *6*, 47–48, doi:10.1103/PhysRevLett.6.47.

Foster, J. C. (1993), Storm time plasma transport at middle and high latitudes, *J. Geophys. Res.*, *98*(A2), 1675–1689, doi:10.1029/92JA02032.

Foster, J. C., and W. J. Burke (2002), SAPS: A new characterization for sub-auroral electric fields, *Eos Trans. AGU*, *83*, 393–394, doi:10.1029/2002EO000289.

Foster, J. C., and H. B. Vo (2002), Average characteristics and activity dependence of the subauroral polarization stream, *J. Geophys. Res.*, *107*(A12), 1475, doi:10.1029/2002JA009409.

Foster, J. C., P. J. Erickson, A. J. Coster, J. Goldstein, and F. J. Rich (2002), Ionospheric signatures of plasmaspheric tails, *Geophys. Res. Lett.*, *29*(13), 1623, doi:10.1029/2002GL015067.

Foster, J. C., et al. (2005), Multiradar observations of the polar tongue of ionization, *J. Geophys. Res.*, *110*, A09S31, doi:10.1029/2004JA010928.

Fujiwara, H., R. Kataoka, M. Suzuki, S. Maeda, S. Nozawa, K. Hosokawa, H. Fukunishi, N. Sato, and M. Lester (2007), Electromagnetic energy deposition rate in the polar upper thermosphere derived from the EISCAT Svalbard radar and CUTLASS Finland radar observations, *Ann. Geophys.*, *25*, 2393–2403, doi:10.5194/angeo-25-2393-2007.

Heppner, J. P., and N. C. Maynard (1987), Empirical high-latitude electric field models, *J. Geophys. Res.*, *92*(A5), 4467–4489, doi:10.1029/JA092iA05p04467.

Huang, C. Y., Y.-J. Su, E. K. Sutton, D. R. Weimer, and R. L. Davidson (2014a), Energy coupling during the August 2011 magnetic storm, *J. Geophys. Res. Space Physics*, *119*, 1219–1232, doi:10.1002/2013JA019297.

Huang, Y., C. Y. Huang, Y.-J. Su, Y. Deng, and X. Fang (2014b), Ionization due to electron and proton precipitation during the August 2011 storm, *J. Geophys. Res. Space Physics*, *119*, 3106–3116, doi:10.1002/2013JA019671.

Kan, J. R., and L. C. Lee (1979), Energy coupling function and solar wind-magnetosphere dynamo, *Geophys. Res. Lett.*, *6*, 577–580, doi:10.1029/GL006i007p00577.

Kelley, M. C., D. J. Knudsen, and J. F. Vickrey (1991), Poynting flux measurements on a satellite: A diagnostic tool for space research, *J. Geophys. Res.*, *96*(A1), 201–207, doi:10.1029/90JA01837.

Lanzerotti, L. J., and A. Hasegawa (1975), High β plasma instabilities and storm time geomagnetic pulsations, *J. Geophys. Res.*, *80*(7), 1019–1022, doi:10.1029/JA080i007p01019.

Li, H., C. Wang, W. Y. Xu, and J. R. Kan (2012), Characteristics of magnetospheric energetics during geomagnetic storms, *J. Geophys. Res.*, *117*, A04225, doi:10.1029/2012JA017584.
Liu, J., T. Nakamura, L. Liu, W. Wang, N. Balan, T. Nishiyama, M. R. Hairston, and E. G. Thomas (2015), Formation of polar ionospheric tongue of ionization during minor geomagnetic disturbed conditions, *J. Geophys. Res. Space Physics*, *120*, 6860–6873, doi:10.1002/2015JA021393.
Lu, G., et al. (1998), Global energy deposition during the January 1997 magnetic cloud event, *J. Geophys. Res.*, *103*(A6), 11,685–11,694, doi:10.1029/98JA00897.
Mannucci, A. J., B. T. Tsurutani, B. A. Iijima, A. Komjathy, A. Saito, W. D. Gonzalez, F. L. Guarnieri, J. U. Kozyra, and A. Skoug (2005), Dayside global ionospheric response to the majorinterplanetary events of October 29-30, 2003 "Halloween Storms", *Geophys. Res. Lett.*, *32*, L12S02, doi:10.1029/2004GL021467.
Milan, S. E., G. Provan, and B. Hubert (2007), Magnetic flux transport in the Dungey cycle: A survey of dayside and nightside reconnection rates, *J. Geophys. Res.*, *112*, A01209, doi:10.1029/2006JA011642.
Moore, T. E., M.-C. Fok, and M. O. Chandler (2002), The dayside reconnection X line, *J. Geophys. Res.*, *107*(A10), 1332, doi:10.1029/2002JA009381.
Newell, P. T., Y. I. Feldstein, Y. I. Galperin, and C.-I. Meng (1996), Morphology of nightside precipitation, *J. Geophys. Res.*, *101*(A5), 10,737–10,748, doi:10.1029/95JA03516.
Nishida, A. (1968), Coherence of geomagnetic DP 2 fluctuations with interplanetary magnetic variations, *J. Geophys. Res.*, *73*(17), 5549–5559, doi:10.1029/JA073i017p05549.
Palmroth, M., H. Koskinen, T. Pulkkinen, and P. Janhunen (2004), Ionospheric power consumption in global MHD simulation predicted from solar wind measurements, *IEEE Trans. Plasma Sci.*, *32*, 1511–1518, doi:10.1109/TPS.2004.830989.
Perreault, W. K., and S.-I. Akasofu (1978), A study of geomagnetic storms, *Geophys. J. R. Astron. Soc.*, *54*, 547–573, doi:10.1111/j.1365-246X.1978.tb05494.
Petrinec, S. M., and C. T. Russell (1996), Near-Earth magnetotail shape and size as determined from the magnetopause flaring angle, *J. Geophys. Res.*, *101*(A1), 137–152, doi:10.1029/95JA02834.
Prolss, G. W. (2006), Subauroral electron temperature enhancement in the nighttime ionosphere, *Ann. Geophys.*, *24*(7), 1871–1885, doi:10.5194/angeo-24-1871-2006.
Richmond, A. D. (2010), On the ionospheric application of Poynting's theorem, *J. Geophys. Res.*, *115*, A10311, doi:10.1029/2010JA015768.
Sato, T. (1959), Morphology of ionospheric F_2 disturbances in the polar regions: A linkage between polar patches and plasmaspheric drainage plumes, *Rep. Ionos. Res. Space Res. Jpn.*, *13*, 91.
Sato, T., and G. F. Rourke (1964), F-region enhancements in the Antarctic, *J. Geophys. Res.*, *69*(21), 4591–4607, doi:10.1029/JZ069i021p04591.
Shue, J.-H., J. K. Chao, H. C. Fu, C. T. Russell, P. Song, K. K. Khurana, and H. J. Singer (1997), A new functional form to study the solar wind control of the magnetopause size and shape, *J. Geophys. Res.*, *102*(A5), 9497–9511, doi:10.1029/97JA00196.
Siscoe, G. L., G. M. Erickson, B. U. Sonnerup, N. C. Maynard, K. D. Siebert, D. R. Weimer, and W. W. White (2000), Deflected magnetosheath flow at the high-latitude magnetopause, *J. Geophys. Res.*, *105*(A6), 12,851–12,857, doi:10.1029/1999JA000268.
Sotirelis, T., P. T. Newell, and C.-I. Meng (1997), Polar rain as a diagnostic of recent rapid dayside merging, *J. Geophys. Res.*, *102*(A4), 7151–7157, doi:10.1029/96JA03564.
Spiro, R. W., R. A. Wolf, and B. G. Fejer (1988), Penetration of high-latitude-electric-field effects to low latitudes during SUNDIAL 1984, *Ann. Geophys.*, *6*(1), 39–50.
Stauning, P. (2007), A new index for the interplanetary merging electric field and geomagnetic activity: Application of the unified polar cap indices, *Space Weather*, *5*, S09001, doi:10.1029/2007SW000311.
Su, Y.-J., M. F. Thomsen, J. E. Borovsky, and J. C. Foster (2001), A linkage between polar patches and plasmaspheric drainage plumes, *Geophys. Res. Lett.*, *28*(1), 111–113, doi:10.1029/2000GL012042.
Torbert, R. B., C. A. Cattell, F. S. Mozer, and C.-I. Meng (1981), The boundary of the polar cap and its relation to electric fields, field-aligned currents, and auroral particle precipitation, in *Physics of Auroral Arc Formation*, *Geophys. Monogr. Ser.*, vol. 25, edited by S.-I. Akasofu and J. R. Kan, 143 pp., AGU, Washington, D. C.
Troshichev, O. A., R. Y. Lukianova, V. O. Papitashvili, F. J. Rich, and O. Rasmussen (2000), Polar cap index (PC) as a proxy for ionospheric electric field in the near-pole region, *Geophys. Res. Lett.*, *27*, 3809–3812, doi:10.1029/2000GL003756.
Tsurutani, B. T. and Gonzalez, W. D. (1997), The interplanetary causes of magnetic storms: A review, in *Magnetic Storms*, edited by B. T. Tsurutani et al., AGU, Washington, D. C., doi:10.1029/GM098p0077.
Valladares, C. E., H. C. Carlson Jr., and K. Fukui (1994), Interplanetary magnetic field dependency of stable sun-aligned polar cap arcs, *J. Geophys. Res.*, *99*(A4), 6247–6272, doi:10.1029/93JA03255.
Valladares, C. E., D. T. Decker, R. Sheehan, D. N. Anderson, T. Bullett, and B. W. Reinisch (1998), Formation of polar cap patches associated with north-to-south transitions of the interplanetary magnetic field, *J. Geophys. Res.*, *103*(A7), 14,657–14,670, doi:10.1029/97JA03682.
Wang, C., J. P. Han, H. Li, Z. Peng, and J. D. Richardson (2014), Solar wind-magnetosphere energy coupling function fitting: Results from a global MHD simulation, *J. Geophys. Res. Space Physics*, *119*, 6199–6212, doi:10.1002/2014JA019834.
Whalen, J. A. (1989), The daytime *F* layer trough and its relation to ionospheric magnetospheric convection, *J. Geophys. Res.*, *94*, 17,169–17,184, doi:10.1029/JA094iA12p17169.
Winningham, J. D., and W. J. Heikkila (1974), Polar cap auroral electron fluxes observed with ISIS 1, *J. Geophys. Res.*, *79*, 949–957, doi:10.1029/JA079i007p00949.